JACS
JOURNAL OF THE AMERICAN CHEMICAL SOCIETY

Article

pubs.acs.org/JACS

"Supersaturated" Self-Assembled Charge-Selective Interfacial Layers for Organic Solar Cells

Charles Kiseok Song,[†] Kyle A. Luck,[‡] Nanjia Zhou,[‡] Li Zeng,[§] Henry M. Heitzer,[†] Eric F. Manley,[†,∥] Samuel Goldman,[⊥] Lin X. Chen,*[,†,∥] Mark A. Ratner,*[,†,‡] Michael J. Bedzyk,*[,‡,§] Robert P. H. Chang,*[,‡] Mark C. Hersam,*[,†,‡] and Tobin J. Marks*[,†,‡]

[†]Department of Chemistry and the Argonne-Northwestern Solar Energy Research Center, Northwestern University, 2145 Sheridan Road, Evanston, Illinois 60208, United States

[‡]Department of Materials Science and Engineering and the Argonne-Northwestern Solar Energy Research Center, Northwestern University, 2220 Campus Drive, Evanston, Illinois 60208, United States

[§]Graduate Program in Applied Physics, Northwestern University, 2220 Campus Drive, Evanston, Illinois 60208, United States

[∥]Chemical Sciences and Engineering Division, Argonne National Laboratory, 9700 South Cass Avenue, Argonne, Illinois 60439, United States

[⊥]Weinberg College of Arts and Science, Northwestern University, 1918 Sheridan Road, Evanston, Illinois 60208, United States

Supporting Information

ABSTRACT: To achieve densely packed charge-selective organosilane-based interfacial layers (IFLs) on the tin-doped indium oxide (ITO) anodes of organic photovoltaic (OPV) cells, a series of Ar_2N-$(CH_2)_n$-$SiCl_3$ precursors with Ar = 3,4-difluorophenyl, n = 3, 6, 10, and 18, was synthesized, characterized, and chemisorbed on OPV anodes to serve as IFLs. To minimize lateral nonbonded -NAr_2···Ar_2N- repulsions which likely limit IFL packing densities in the resulting self-assembled monolayers (SAMs), precursor mixtures having both small and large n values are simultaneously deposited. These "heterogeneous" SAMs are characterized by a battery of techniques: contact angle measurements, X-ray reflectivity, X-ray photoelectron spectroscopy, ultraviolet photoelectron spectroscopy (UPS), cyclic voltammetry, and DFT computation. It is found that the headgroup densities of these "supersaturated" heterogeneous SAMs (SHSAMs) are enhanced by as much as 17% versus their homogeneous counterparts. Supersaturation significantly modifies the IFL properties including the work function (as much as 16%) and areal dipole moment (as much as 49%). Bulk-heterojunction OPV devices are fabricated with these SHSAMs: ITO/IFL/poly[[4,8-bis[(2-ethylhexyl)oxy]benzo[1,2-*b*:4,5-*b*′]dithiophene-2,6-diyl][2-[[(2-ethylhexyl)oxy]carbonyl]-3-fluorothieno[3,4-*b*]thiophenediyl]]:phenyl-C_{71}-butyric acid methyl ester (PTB7:$PC_{71}BM$)/LiF/Al. OPVs having SHSAM IFLs exhibit significantly enhanced performance (PCE by 54%; V_{oc} by 35%) due to enhanced charge selectivity and collection, with the PCE rivaling or exceeding that of PEDOT:PSS IFL devices −7.62%. The mechanism underlying the enhanced performance involves modified hole collection and selectivity efficiency inferred from the UPS data. The ITO/SAM/SHSAM surface potential imposed by the dipolar SAMs causes band bending and favorably alters the Schottky barrier height. Thus, interfacial charge selectivity and collection are enhanced as evident in the greater OPV V_{oc}.

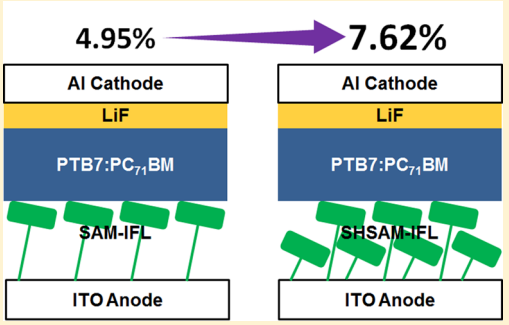

INTRODUCTION

Diverse properties of surfaces can be chemically tailored via the chemisorption of self-assembled monolayers (SAMs). Thus, SAMs have been used in organic electronics applications such as organic photovoltaics,[1−6] thin-film transistors,[7−9] and organic/polymer light-emitting diodes.[10−13] Using SAM surface modification for detecting chemicals[14,15] and biological agents[16−18] has advanced sensor technologies as well. SAM precursor molecules typically consist of three parts: the head, tail, and anchor groups (e.g., Figures 1 and 2). These groups can also substantially modulate surface properties such as hydrophobicity,[15,19,20] electrical conductivity,[21−23] and charge injection/collection selectivity through the film.[1,2,10] For example, on metal oxide substrates,[1,24] SAMs can significantly influence surface energy,[25,26] work function,[2,27] polymer adhesion,[24,28] and charge transfer (CT) rates to the oxide band structure.[1,29] Functionalized surface properties can also be modulated via SAM packing densities and film thicknesses,[1,21,30,31] which can be tuned by the SAM headgroup chemical properties and the tail and anchor group architectures. For optoelectronics applications such as photovoltaics, high packing densities and substantial dipole moments in the constituent molecules of electrode coatings have been shown to enhance device performance by

Received: August 18, 2014
Published: November 24, 2014

 © 2014 American Chemical Society dx.doi.org/10.1021/ja508453n | J. Am. Chem. Soc. 2014, 136, 17762−17773

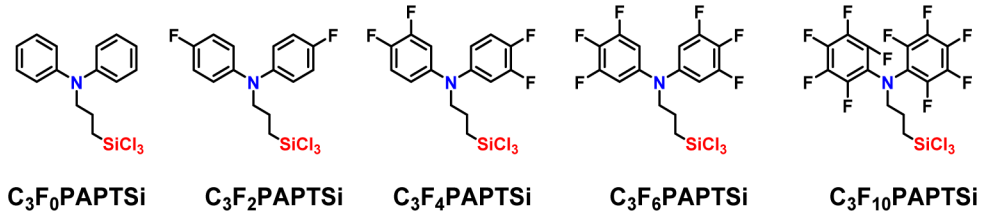

Figure 1. Molecular structures of the C_3F_nPAPTSi series of IFL precursors examined in the previous study. The subscripts after C and F in the labels indicate the number of methylene units in the tail chain and the number of F atoms on the headgroup, respectively. Note that all molecules have same chain length.

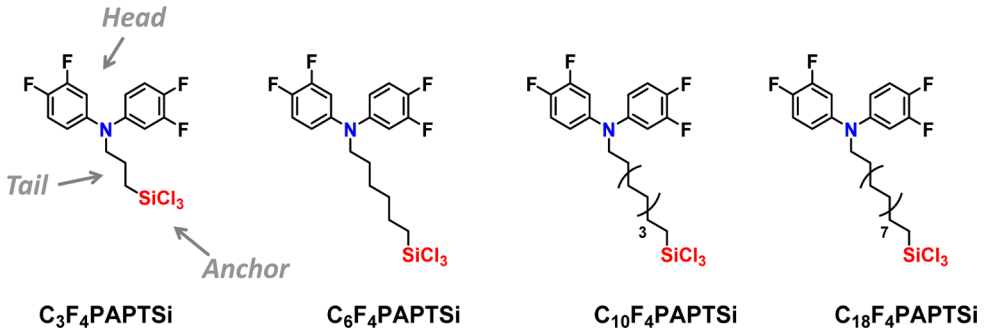

Figure 2. Structures of representative SAM precursors used in this study. The subscripts after C and F in the labels indicate the number of methylene units in the tail chain and the number of F atoms on the headgroup, respectively. Note that all molecules have the same headgroups.

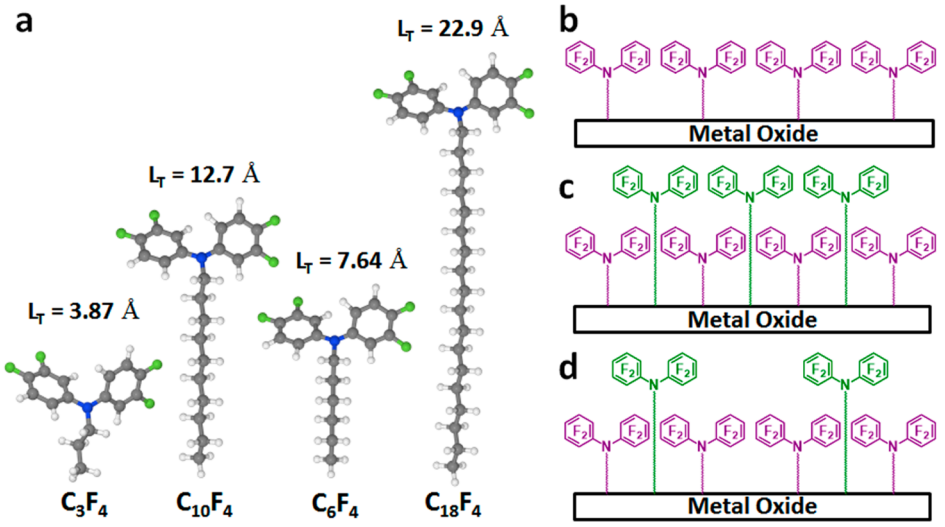

Figure 3. Schematic chemisorption of SAM precursors having different tail lengths (L_T) on electrode surfaces to form a second headgroup layer above the first layer of a thinner SAM. (a) DFT-optimized geometries of simplified (C−H terminated) SAM precursors and corresponding abbreviations. Gray, blue, green, and white spheres represent C, N, F, and H atoms, respectively. Schematics of (b) saturated homogeneous SAM, (c) supersaturated heterogeneous SAM (SHSAM), and (d) SHSAM derived from a different precursor ratio.

enhancing charge collection rates.[1,3,32,33] Specifically, manipulating charge collection rates via SAM constituent dipole moments at a fixed molecular length (Figure 1) has been demonstrated in results from this laboratory.[1] From this study, the CT kinetics of homogeneous dipolar SAM were found to be directly proportional to the dipole moment and the packing density of precursor molecules. On the less positive side, many SAM precursors intended for these applications form monolayers with suboptimal surface densities due to bulky headgroups,[1,34,35] including molecules in Figure 1. This can limit the effectiveness of the SAM physicochemical properties.

With the objective of overcoming SAM densification limitations arising from sterically encumbered headgroups, we investigated mixed SAMs derived from modifications of precursor molecule **C_3F_4PAPTSi** because this precursor afforded the highest OPV metrics and dipole moment.[1] A series of molecules was designed with identical headgroups and anchor groups to **C_3F_4PAPTSi** for a constant dipole moment while tail group lengths were varied, as shown in Figures 2 and 3a. If the surface density is limited by headgroup encumbrance (Figure 3b), we envisioned that coadsorbing a second precursor with an identical redox-active headgroup but a longer tail might relieve lateral steric repulsions and increase SAM densities (Figure 3c). In principle, a precursor with a longer tail group should bind to the substrate surface, occupying vacant sites between shorter SAM constituents, and forming an additional headgroup layer.

dx.doi.org/10.1021/ja508453n | J. Am. Chem. Soc. 2014, 136, 17762−17773

Analogous approaches, but not involving electroactive components, have been reported with mixtures of bulky and slender precursors by Chidsey,[30] Sabatani,[36] and Chailapakul.[37] Such heterogeneous SAMs are expected to be "supersaturated" in surface headgroup densities; we term this SAM variant a supersaturated heterogeneous SAM, a "SHSAM".

To investigate the consequences of anode SHSAMs on OPV performance, two SAM precursors having different DFT-computed molecular lengths (L_M's), **C_3F_4PAPTSi** (L_M = 7.98 Å) and **$C_{10}F_4$PAPTSi** (L_M = 16.7 Å), were chosen as models (Figure 3). The DFT analysis confirms that the length of the **$C_{10}F_4$PAPTSi** tail group (L_T; L_T = 12.7 Å) is sufficiently long to position its headgroup above the **C_3F_4PAPTSi** SAM surface. This novel SAM variant combining short- and long-tailed precursors with identical electroactive headgroups is fabricated and characterized here by a battery of chemical and physicochemical methods. It will be seen that SHSAM modulation of IFL electronic properties is significantly greater than by the homogeneous SAM counterparts because of increased packing density and additional intermolecular dipolar interactions (Figure 3c). Next, bulk-heterojunction organic photovoltaic (BHJ OPV) cells are fabricated with SHSAM IFLs. Organosilane BHJ OPV IFLs were previously studied in as hole-collecting IFLs in this laboratory,[1] and it was shown that the interplay of homogeneous SAM packing density, dipole moment, and heterogeneous electron transfer rates strongly influence OPV performance metrics. In this contribution, BHJ OPVs having conventional tin-doped indium oxide (ITO)/anode IFL/active layer/LiF/Al architectures (Supporting Information Figure S1) with a poly[[4,8-bis[(2-ethylhexyl)oxy]-benzo[1,2-*b*:4,5-*b*′]dithiophene-2,6-diyl][3-fluoro-2-[(2-ethylhexyl)-carbonyl]thieno[3,4-*b*]thiophenediyl]]:phenyl-C_{71}-butyric acid methyl ester (PTB7:$PC_{71}BM$) active layer are fabricated with hole-collecting/electron-blocking IFL = homogeneous SAM and SHSAM IFL functionalized ITO anodes, and characterized. Representative OPVs having SHSAM IFLs exhibit significantly greater performance versus comparable devices having either homogeneous SAM or PEDOT:PSS IFLs. Finally, comments are made regarding the implications of these results for other SAM-modified device technologies.

EXPERIMENTAL SECTION

Self-Assembled Monolayer Precursor Synthesis. All reactions were carried out with strict Schlenk protocol. All reagents were from Sigma-Aldrich and used as received unless otherwise indicated. Predried hexane and toluene from Sigma-Aldrich were dried further by passing through a Grubbs column, and anhydrous acetonitrile was used for all syntheses and analyses. ^{1}H and ^{19}F NMR spectra were measured at 500 MHz by Agilent INOVA 500 and at 376 MHz by Agilent DDR2 instruments, respectively; all ^{13}C NMR spectra were measured at 126 MHz on a Bruker AVANCE III instrument with a direct cryoprobe. High-resolution mass spectra (HRMS) were measured with a Waters GCT-Premier mass spectrometer with an Agilent 7910 series GC and EI ionization source. Elemental analyses (EAs) were determined at Midwest Microlabs, LCC., and the theoretical and experimental values are provided. The common precursor molecule to all SAM precursors, 3,4-difluoro-*N*-(3,4-difluorophenyl)benzenamine, 3,4-difluoro-*N*-(3,4-difluorophenyl)-*N*-2-propen-1-ylbenzenamine, and *N*-(3-trichlorosilylpropyl)-3,4-difluoro-*N*-(3,4-difluorophenyl)-benzenamine (**C_3F_4PAPTSi**) were synthesized as described in the previous study.[1] Detailed synthetic procedures for, and characterizations of, the SAM precursors are described in the Supporting Information (S2).

Self-Assembled Monolayer Characterization. The SAM-grafted and air-plasma-treated glass/ITO (ITO/SAM) and Si(100)/SiO_2 (Si/SiO_2/SAM) substrates were characterized by contact angle (CA) measurements, atomic force microscopy (AFM), X-ray reflectivity (XRR), X-ray photoelectron spectroscopy (XPS), ultraviolet photoelectron spectroscopy (UPS), and cyclic voltammetry (CV). Each deposition batch yielded 8 coated substrates, and all analyses were carried out with coated substrates from the same batch to minimize batch-to-batch variations. The glass/ITO or Si(100)/SiO_2 substrates grafted with **C_3F_4PAPTSi**, **C_6F_4PAPTSi**, **$C_{10}F_4$PAPTSi**, and **$C_{18}F_4$PAPTSi** are designated ITO or Si/SiO_2/**C_3F_4**, /**C_6F_4**, /**$C_{10}F_4$**, and /**$C_{18}F_4$**, respectively, and the glass/ITO or Si(100)/SiO_2 substrates grafted with 1:1, 3:1, and 5:1 solution ratios of **C_3F_4PAPTSi** and **$C_{10}F_4$PAPTSi** are named ITO or Si/SiO_2/**1:1**, /**3:1**, and /**5:1**, respectively. Finally, the names **bare** and ITO/**PEDOT:PSS** are used for solvent-cleaned glass/ITO substrates and glass/ITO substrates coated with PEDOT:PSS, respectively. Detailed SAM grafting methods and characterizations are described in the Supporting Information (S6).

OPV Device Fabrication. The active layer solution is prepared by dissolving poly[[4,8-bis[(2-ethylhexyl)oxy]benzo[1,2-*b*:4,5-*b*′]dithiophene-2,6-diyl][2-[[(2-ethylhexyl)oxy]carbonyl]-3-fluorothieno[3,4-*b*]thiophenediyl]]:phenyl-C_{71}-butyric acid methyl ester (PTB7:$PC_{71}BM$) in a 97.0%/3.0% (by volume) solution of anhydrous chlorobenzene:1,8-diiodooctane (Sigma-Aldrich) at a polymer loading of 10 mg/mL (2:3 by wt). To ensure complete dissolution, this solution is allowed to stir for 2 days at 70 °C under an N_2 atmosphere. PTB7 and $PC_{71}BM$ were obtained from 1-Material and American Dye Source, respectively. The PTB7:$PC_{71}BM$ solution is spin-coated (30 s at 1100, 1200, and 1500 rpm) onto the ITO/**C_nF_n**, ITO/***n*:1**, **bare**, and ITO/**PEDOT:PSS** substrates. The contact area for the to-be deposited electrodes is defined by cleaning with a dry cotton swab. LiF (1 nm, 0.1 Å/s) and Al (100 nm, ∼1.5 Å/s) were then deposited via vacuum thermal evaporation with a shadow mask to yield 4 OPV devices per substrate (0.20 cm × 0.35 cm, device area = 0.07 cm^2 each). Before exposure to ambient environment, the completed devices are encapsulated using a cover glass with UV-curable ELC-2500 epoxy and cured in a UV chamber (Electro-Lite) for 10 min.

OPV Characterization. A Spectra-Nova Class A Solar Simulator, equipped with a 500 W Xe arc lamp, simulated AM1.5G light from 400 to 1100 nm, was used to test the OPV devices. To bring the spectral mismatch close to unity, the light source was calibrated with an NREL-certified monocrystalline Si diode equipped with a KG3 filter. The $J-V$ curve data were obtained from a Keithley 2400 digital source meter. External quantum efficiency (EQE) measurements were performed with an Oriel Model QE-PV-SI instrument (Newport Instruments) equipped with a NIST-certified Si-diode, a Merlin lock-in amplifier, and an optical chopper. Monochromatic light is generated from a 300 W Xe arc lamp. The EQE data were integrated using the Open Photovoltaics Analysis Platform program[38] and used to correct the short circuit current density (J_{sc}) data obtained by the solar simulator. Corrections were typically on the order of ∼9%.

RESULTS

In this section, the syntheses and structures of the new SAM precursors are described first, followed by their chemisorption properties. The physicochemical characteristics of the SAM structures are then presented, including information on the surface energy, surface composition, as well as thickness and packing density (Γ). The work function (Φ_s), hypothetical/simulated areal dipole moments ($\mu_{A,hyp}/\mu_{A,sim}$), and heterogeneous electron transfer rate constants (k_s) of the SAMs are then obtained from the experimental data and computational modeling. Finally, the photovoltaic performance of the BHJ OPVs fabricated using the SAMs and SHSAMs as anodic IFLs is discussed in light of the observed trends in the ITO/SAM and SHSAM properties.

Interfacial Layer Fabrication. *SAM and SHSAM Precursor Synthesis and Characterization.* The tetrafluorodiarylamine, the tetrafluorodiarylalkylamines, and corresponding **C_nF_4PAPTSi** SAM precursor reagents were synthesized via the

dx.doi.org/10.1021/ja508453n | J. Am. Chem. Soc. 2014, 136, 17762−17773

Scheme 1. Synthetic Routes to C_nF_4PAPTSi SAM and SHSAM Precursors[a]

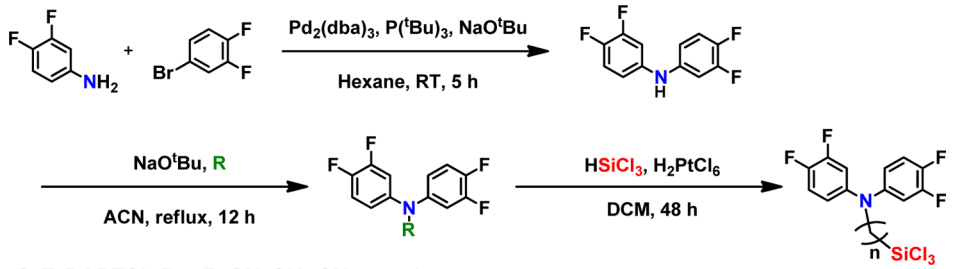

C_3F_4PAPTSi: R = $BrCH_2CH{=}CH_2$, n = 3

C_6F_4PAPTSi: R = $Br(CH_2)_4CH{=}CH_2$, n = 6

$C_{10}F_4$PAPTSi: R = $Br(CH_2)_8CH{=}CH_2$, n = 10

$C_{18}F_4$PAPTSi: R = $Br(CH_2)_{16}CH{=}CH_2$, n = 18

[a]Here, *n* nomenclature denotes the number of C atoms in the alkyl chain.

pathways in Scheme 1. The products were purified by silica gel column chromatography where applicable. The structure and purity of each tetrafluorodiarylalkylamine intermediate was confirmed by ^{1}H, ^{13}C, and ^{19}F NMR coupled with HRMS and C, H, and N elemental analyses. The purities were determined to be >95%. After hydrosilylation (Scheme 1), the **C_nF_4PAPTSi** compounds were also analyzed by ^{1}H, ^{13}C, and ^{19}F NMR spectroscopy, and their isomeric purities (**C_3F_4PAPTSi**) and/or conversion efficiencies (**C_6F_4PAPTSi**, **$C_{10}F_4$PAPTSi**, and **$C_{18}F_4$PAPTSi**) were determined to be ≥85%, with the major impurities assigned to C═C isomerization and hydrogenation byproducts,[39] or to unreacted starting material. Note that further purification by recrystallization or column chromatography is not possible because of the oily nature of the products and reactive nature of the $-SiCl_3$ moieties. The ^{1}H, ^{13}C, and ^{19}F NMR spectra of all new compounds are provided in the Supporting Information.

SAM Growth Optimization. Previously,[1] it was determined that submerging solvent-cleaned, AP-treated glass/ITO substrates in 0.025 M SAM precursor solutions in anhydrous toluene for 24 h was sufficient to saturate the surface coverage. However, after additional drying of the toluene, XRR analysis indicates that Γ does not completely saturate within the first 24 h of immersion. Thus, in this study, the saturation immersion time was extended and found to be ∼31 h, and Γ of a model system, $Si/SiO_2/$**C_3F_4** (3.3×10^{-10} mol/cm^2), is then comparable to that achieved in the previous work (3.3×10^{-10} mol/cm^2) when measured by XRR (see below). The origin of the slightly more sluggish saturation process in the present work is attributed to the lower water concentration in the more extensively dried toluene used for SAM grafting. The sensitivity of oraganosilyltrichloride SAM formation kinetics on Si/SiO_2 to grafting solution water concentrations has been reported elsewhere.[40]

Interfacial Layer Characterization. *SAM Surface Composition.* The surface atomic compositions of the ITO/SAMs were determined by XPS. The atomic % of C, N, Si, and F and the F/N ratios (3.8 on average) determined from XPS closely match the expected stoichiometric F/N ratio (4.0). Some variations are observed in the C ratios which are attributed to surface contamination from atmospheric exposure during substrate transportation. Experimental data are plotted in Supporting Information Figure S4 and tabulated in Supporting Information Table S1.

SAM Surface Energy. The total surface energy, consisting of both dispersive and polar components, was determined from the measured CAs (Supporting Information Figure S5). The dispersive and polar energy components (Figure 4) were

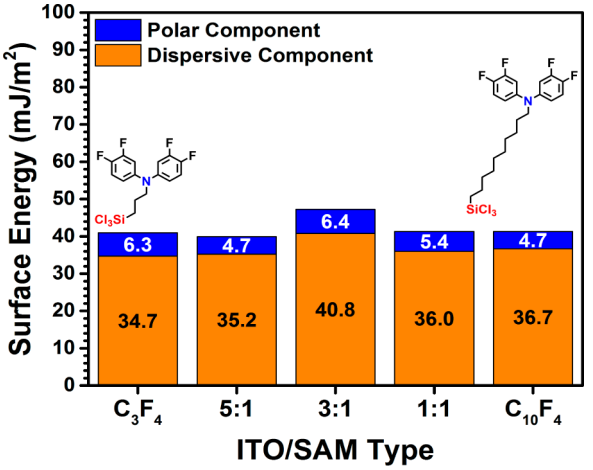

Figure 4. Surface energies of ITO/SAMs/SHSAMs. 1:1, 3:1, and 5:1 represent the molar ratio of **C_3F_4PAPTSi** to **$C_{10}F_4$PAPTSi** in grafting solutions. The total surface energy can be obtained by summing the polar (blue) and dispersive (orange) components.

calculated from the CAs measured for two liquids, water and diiodomethane,[26] on the basis of Young's equation and the Owens−Wendt−Kaelble equation[41]

$$\gamma_L(1 + \cos\theta) = 2\left(\sqrt{\gamma_S^P\gamma_L^P} + \sqrt{\gamma_S^D\gamma_L^D}\right)$$

where γ_L denotes the total surface energy measured by the pendant drop method,[25] θ denotes the CA, γ denotes the surface energy, superscripts P and D denote the polar and dispersion components, respectively, and the subscripts S and L denote the solid and probe liquid, respectively. The total surface energy ranges from 39.9 to 47.2 mJ/m^2. Except for ITO/**3:1**, the surface energy variation among the ITO/SAM and SHSAM is only ∼6%. ITO/**3:1** has the highest surface energy, which is ∼11.5% greater than the SAM with the next greatest surface energy, ITO/**C_6F_4**. These differences in γ are attributed to microstructural and dipolar interactions within the SAMs, as will be discussed further below. Overall, the total surface energies of the ITO/SAM and SHSAM are ∼40% lower than the AP-treated ITO (γ^D = 30.3 mJ/m^2, γ^P = 43.2 mJ/m^2, γ^T = 73.5 mJ/m^2),[1] or **PEDOT:PSS** (γ^D = 40.6 mJ/m^2, γ^P = 30.6 mJ/m^2, γ^T= 71.2 mJ/m^2).[42] The lower

dx.doi.org/10.1021/ja508453n | J. Am. Chem. Soc. 2014, 136, 17762−17773

Table 1. Measured ITO/SAM and ITO/SHSAM Morphology, Thickness, and Packing Density

IFL	roughness[a] (nm)	thickness[b] (Å)	tilt angle[d] (deg)	e density[b] (e/Å^3)	footprint[b] (Å^2/molecule)	Γ_{CV}[a] / Γ_{XRR}[b] (10^{-10} mol/cm^2)
C_3F_4	2.44	$7.5^{+1.0}_{-0.7}$	37^{+7}_{-11}	$0.37^{+0.10}_{-0.10}$	50^{+8}_{-19}	2.94 ($\pm$0.08)/$3.3^{+2.1}_{-0.4}$
C_6F_4	1.66	$9.8^{+0.5}_{-0.1}$	38^{+1}_{-3}	$0.40^{+0.06}_{-0.12}$	39^{+14}_{-3}	3.09 ($\pm$0.04)/$4.2^{+0.4}_{-0.9}$
$C_{10}F_4$	2.30	$9.0^{+1.3}_{-0.4}$	59^{+1}_{-5}	$0.41^{+0.06}_{-0.13}$	52^{+11}_{-5}	2.92 ($\pm$0.03)/$3.2^{+0.4}_{-0.6}$
$C_{18}F_4$	2.00	$11.1^{+0.5}_{-0.1}$	66^{+0}_{-1}	$0.41^{+0.04}_{-0.13}$	55^{+21}_{-9}	2.05 ($\pm$0.02)/$3.3^{+0.6}_{-0.8}$
5:1	1.55	$7.4^{+0.6}_{-0.1}$	NA[c]	$0.41^{+0.05}_{-0.13}$	NA[c]	3.42 ($\pm$0.03)/NA[c]
3:1	1.54	$8.2^{+0.6}_{-0.2}$	NA[c]	$0.41^{+0.05}_{-0.13}$	NA[c]	2.93 ($\pm$0.09)/NA[c]
1:1	1.72	$8.2^{+0.6}_{-0.6}$	NA[c]	$0.41^{+0.10}_{-0.13}$	NA[c]	3.23 ($\pm$0.07)/NA[c]
bare ITO	1.34	NA	NA	NA	NA	NA

[a]Data on ITO. [b]Data on Si/SiO_2. [c]Data not be obtained because of the unknown surface composition of heterogeneous SAMs. [d]Tilt angles estimated from XRR thickness data and molecular lengths computed from the DFT optimized molecular geometry.

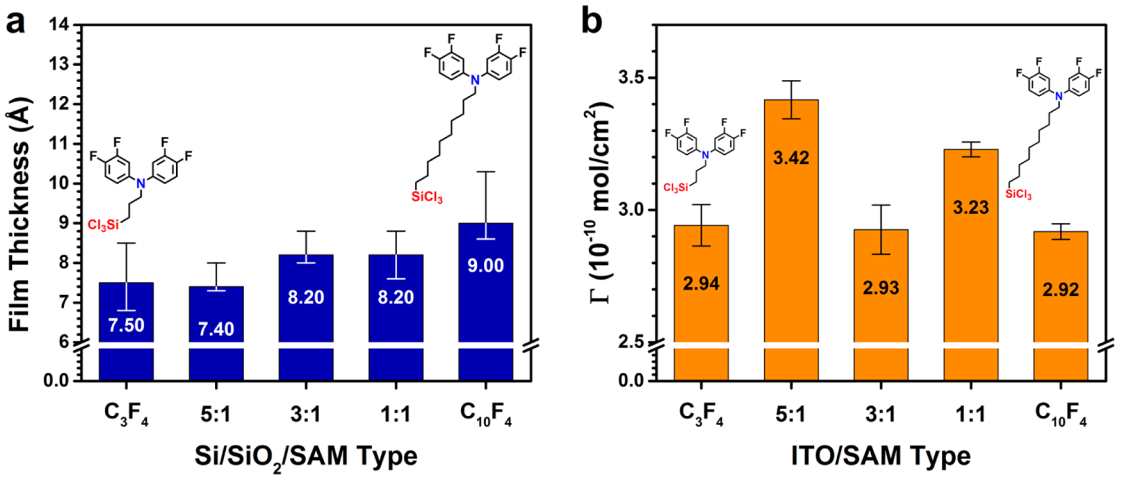

Figure 5. (a) XRR-derived film thicknesses of the indicated Si/SiO_2/SAMs/SHSAMs. (b) CV-derived surface packing densities of the indicated ITO/SAMs/ITO/SHSAMs. Here, 1:1, 3:1, and 5:1 represent SAMs chemisorbed from solutions of 1:1, 3:1, and 5:1 molar ratio of **C_3F_4PAPTSi**:**$C_{10}F_4$PAPTSi**, respectively. Note that the heterogeneous ITO/SHSAMs, 1:1, 3:1, and 5:1, are somewhat thinner than **$C_{10}F_4$**, and have similar or greater packing densities than the homogeneous SAMs, **C_3F_4** and **$C_{10}F_4$**. Film thicknesses and the packing densities are determined by XRR and by integrating the first oxidation curve in the CV scans, respectively.

ITO/SAM and SHSAM total surface energies mostly originate from reduction in the polar component, which should oppose the dewetting of an organic material on the surface, such as the active layer of a BHJ OPV due to surface energy mismatch.[24,28,43−46]

SAM Morphology. The SAM surface morphological properties, such as the rms roughnesses, thicknesses, and average molecular tilt angles, were determined by AFM, XRR, and DFT-assisted computation. The surface roughness features in 5 μm × 5 μm areas determined by AFM indicate that no significant morphological changes occur after grafting the ITO substrates with the SAMs or SHSAMs (Supporting Information Figure S6). The rms surface roughness of each of the ITO/SAM and SHSAM (Table 1) is slightly greater than that of bare ITO (~1.3 nm). Also, compared to a homogeneous SAM, the heterogeneous SAMs are somewhat smoother. Any increased rms roughness upon SAM grafting presumably originates from the particular SAM tail dimensions rather than the ITO roughness,[47] which are too short to fill valleys and planarize the rough ITO surface topography. In contrast, longer tail groups should facilitate planarization and yield smoother surfaces. Indeed, the homogeneous SAMs with longer tails are found in general to exhibit lower rms roughnesses (Table 1). Furthermore, the difference in roughness between homogeneous and SHSAMs presumably originates from the availability of the variable chain lengths. The addition of a SAM precursor with a different chain length plausibly helps to flatten the surface by filling gaps inaccessible to the other SAM precursor (Supporting Information Figure S2).

In agreement with the AFM results, XRR analysis also reveals that the Si/SiO_2/SAM and SHSAM surface roughnesses (~3.3 Å, Supporting Information Table S2) do not differ greatly among SAM variants. Since the Si(100)/SiO_2 surface is very smooth (rms roughness ~1.2 Å), there are no gaps to be filled by longer chains, thus resulting in a more uniform topology. The near constant surface roughnesses of the Si/SiO_2/SAMs and SHSAMs also strengthen the argument that the differences in roughness among the ITO/SAMs and SHSAMs largely originate from the ITO surface roughness.

Finally, the XRR analysis reveals that the film thicknesses range from 7.4 to 11.1 Å (Figure 5a). For homogeneous SAMs, the film thicknesses generally increase from 7.5 to 11.1 Å as the chain length increases from 3 to 18 methylene groups. A similar trend was reported by Chidsey:[21] organosilane SAM-coated Si(111). In the case of the SHSAMs, an intriguing film thickness variation is observed as the ratio of SAM precursors in the grafting solution is changed. It is found that ITO/**1:1** (8.2 Å) and ITO/**3:1** (8.2 Å) have similar film thicknesses followed by ITO/**5:1** (7.4 Å) despite increased SHSAM Γs compared to homogeneous SAMs. These heterogeneous SAM thickness variations may reflect, among other factors, in-film dipolar interactions[16,48,49] (see below). Note that no discernible domains are observed in AFM images (Supporting Information Figure S6) and from XRR data (Supporting Information Figure S7 and Table S2). The AFM

Table 2. Computed and Measured ITO/SAM and SHSAM Electronic Properties

SAM	μ^a (Debye)	$\mu_{A,hyp}{}^a/\mu_{A,sim}{}^a$ (Debye/nm^2)	ε^a	$\Phi_s{}^{b,c}$ (eV)	ITO $VB_{SB}{}^{b,c}$ (eV)	$VBM^{b,c}$ (eV)	$k_s{}^b$ (s^{-1})
C_3F_4	3.62	−7.22/−0.86	2.11	4.65	3.09	1.28	1.27 (±0.04)
C_6F_4	3.84	NA	NA	4.45	3.18	1.50	0.743 (±0.087)
$C_{10}F_4$	3.88	NA/−0.98	1.73	4.35	3.27	1.64	1.49 (±0.09)
$C_{18}F_4$	3.91	NA	NA	4.30	3.16	1.46	1.25 (±0.04)
5:1	NA[d]	NA	NA	5.03	2.96	1.18	0.988 (±0.010)
3:1	NA[d]	NA/−1.28[e]	1.58[e]	4.76	3.13	1.45	0.976 (±0.025)
1:1	NA[d]	−11.7/−1.21[e]	1.72[e]	4.78	3.11	1.37	1.04 (±0.07)

[a]DFT computed property. [b]Experimental data. [c]Standard deviation <0.1 eV. [d]Data could not be obtained because of the unknown surface compositions of SHSAMs. [e]Surface composition assumed equal to precursor mole fractions in the corresponding SAM grafting solution.

image does not reveal noticeable features other than the surface pattern observed from a bare ITO substrate, and XRR determined surface roughnesses are virtually invariant throughout Si/SiO_2/SAM and SHSAM series implying that SHSAMs are mixed uniformly. This result also argues that deriving SHSAM surface compositions from the morphological data is necessarily imprecise.

SAM Packing Density. The Γs of the chemisorbed SAMs and SHSAMs were determined by both cyclic voltammetry (CV) and X-ray reflectivity (Γ_{XRR}) measurements.[10] In the former, the number of electrons transferred during the oxidation process (Supporting Information Figure S8) was determined by taking the quotient of the integrated fitted oxidation peak for the first forward scan by the product of the scan rate, electrode area, and Faraday's constant. The oxidation peaks were fitted using the Extreme peak fitting package from OriginLab 9.1.0 Sr1, and derived estimated uncertainties are included in Table 1. Assuming one electron is transferred per SAM molecule, Γ_{CV} is determined to be in the range 2.05×10^{-10} to 3.09×10^{-10} mol/cm^2 for the homogeneous SAMs and 2.93×10^{-10} to 3.23×10^{-10} mol/cm^2 for the SHSAMs, with <3% uncertainties from the fitted curves. The CV scans are shown in Supporting Information Figure S8. The general decrease in Γ of the homogeneous SAMs with increasing chain length is similar to trends reported elsewhere.[50] The Γs of the homogeneous SAMs on the Si(100)/SiO_2 substrates were also calculated from the XRR data (Supporting Information Figures S7 and S9) by multiplying the volumetric electron density by the XRR-derived film thickness data, yielding the areal electron density. Next, the molecular footprint, the area occupied by the anchored SAM molecule on the substrate surface, was calculated by dividing the total number of electrons of the corresponding molecule by this areal electron density. The inverse of the obtained footprints yields Si/SiO_2/SAM Γ_{XRR} values, which generally agree well with the electrochemically derived Γ_{CV} values (Figure 5b and Supporting Information Figure S9, and Table 1). Finally, the SAM molecular tilt angles are estimated by dividing the molecular length calculated from the DFT-optimized geometry by the corresponding film thickness. See the Supporting Information (S7) for a discussion of the error analysis.

The observed differences between the homogeneous SAM and SHSAM packing densities in Figure 5b and Table 1 can be explained from the computational results. For example, a hypothetical cluster of four molecules based on the DFT-optimized geometries (Supporting Information Figure S2) indicates why the heterogeneous ITO/**n:1**s have greater packing densities. By allowing the headgroups to overlap in the SHSAMs, more molecules can be packed in a unit area (3.02 molecules nm^{-2}) versus an analogous homogeneous SAM (1.51 molecules nm^{-2}).

SAM Electronic Properties. The electronic structure properties of the ITO/SAM and SHSAM surfaces, namely, molecular dipole moment (μ), areal dipole moment (μ_A), dielectric constant (ε), work function (Φ_s), valence band maximum (VBM), ionization potential (IP), and heterogeneous electron transfer rate constant (k_s), were determined by DFT computation, UPS, and CV, respectively. The molecular dipole moments, hypothetical areal dipole moments ($\mu_{A,hyp}$), and IPs were computed from the DFT-optimized molecular geometries. The simulated areal dipole moments ($\mu_{A,sim}$) and ε values were calculated by finite difference techniques (Supporting Information S12),[51] constructing a series of unit cells based on Γ_{CV} with the homogeneous SAM precursors **C_3F_4PAPTSi** and **$C_{10}F_4$PAPTSi**, and the heterogeneous SAM precursors with 1:1 and 3:1 molar ratios of **C_3F_4PAPTSi** and **$C_{10}F_4$PAPTSi**. From these calculations, the SHSAMs are found to have significantly larger hypothetical ($\mu_{A,hyp}$ = −11.7 vs −7.22 D/nm^2) and simulated areal dipole moments ($\mu_{A,sim}$ = −1.21, and −1.28 vs −0.86, and −0.98 D/nm^2) than the homogeneous SAMs (Table 2). The differences in the $\mu_{A,hyp}$ and $\mu_{A,sim}$ magnitudes originate, not unexpectedly, from differences in the computational methods and assumptions. Most importantly, the trends in $\mu_{A,hyp}$ and $\mu_{A,sim}$ are very similar.

Interestingly, the estimated ε values of the simulated heterogeneous SHSAMs (1.72 and 1.58) are found to be slightly smaller than those of the simulated homogeneous SAMs (2.11 and 1.73). The differences in μ_As and εs appear to arise from the increased Γs and in-film dipolar interactions to be discussed further below and in the Supporting Information (S21). The IPs were also measured in an electrolyte solution (0.1 M $TBA^+PF_6^-$ in acetonitrile) by CV (Supporting Information Figure S8), in which the peak of the oxidation potential (E_{Ox}) with respect to the ferrocene redox potential ($Fc_{1/2}$, 630 mV vs NHE)[52] is referenced against the ferrocene work function (5.1 eV)[53] as in the equation below.

$$IP = -e[E_{Ox} - Fc_{1/2}] - 5.1\ eV$$

The UPS-derived IPs and spectroscopic data (Supporting Information Figure S10) were also used to derive the work function (Φ_s), VBM, and the valence band of the bulk ITO substrate (VB_{SB}). Φ_s was determined from the difference between the secondary electron cutoff (SECO), the highest binding energy, and the He I source energy (21.22 eV).[54,55] The VBM values of the ITO/SAMs relative to the Fermi level (E_F; 0.0 eV) were determined from the onset of the lowest binding energy. The VB_{SB} values were determined from the onset of the second lowest binding energy based on the VBM of bare ITO. The IP was then calculated from the sum of the work function and the VBM.[54,56] Unfortunately, since all the ITO/SAM IPs are very similar (<4% difference), electrochemical methods cannot

dx.doi.org/10.1021/ja508453n | J. Am. Chem. Soc. 2014, 136, 17762−17773

be used to accurately estimate the SHSAM composition. The heterogeneous electron transfer constants (k_s) for the ITO/SAMs and SHSAMs were determined from CV experiments by varying scan rate (ν) from 10 to 79 433 mV/s in the presence of Fc (0.002 M) as the redox probe. A Tafel plot (Supporting Information Figure S11) was then constructed from the data, and k_s values were obtained as described in the Supporting Information (S18). Dipole moment, work function, VBM, IP, and k_s data from the various measurements are summarized in Table 2 and Figure 6.

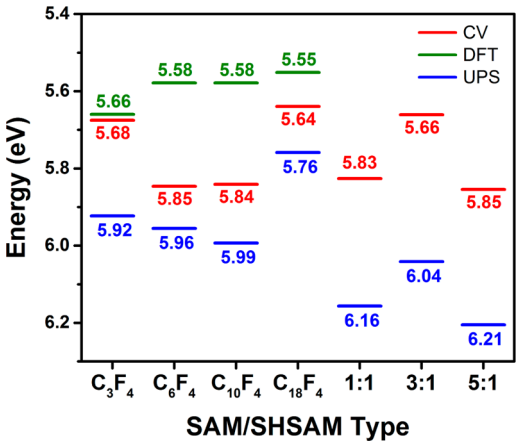

Figure 6. SAM/SHSAM IP values determined from CV (red), DFT (green), and UPS (blue) analyses. DFT methods could not be used to determine the IPs of heterogeneous SAMs.

SAM Adhesion and Chemical Stability. A modified tape test for the adhesion strength of the ITO/SAMs according to the ASTM D3359-09e2 guideline reveals that the present SAMs are tightly bonded to the ITO substrates. The aqueous CA measurements before and after the tape test are virtually identical within experimental error. Similar results are obtained for substrates immersed in hot water for 1 h. No differences are observed in CA measurements before and after immersion in hot water. CA image and data for the SAM and SHSAM stability tests are summarized in Supporting Information Figure S12 and Table S4, respectively.

SAM IFL Effects on OPV Response. PTB7:$PC_{71}BM$ bulk-heterojunction OPV cells were fabricated with the glass/ITO/IFL anodes and characterized using procedures described earlier.[1,57] The averaged $J-V$ curves of the six best-performing device types with two different substrates, corrected by EQE measurements, are shown in Figure 7a. The open circuit voltage (V_{oc}), short circuit current density (J_{sc}), fill factor (FF), and power conversion efficiency (PCE) data for selected devices are summarized in Table 3, and with data analysis statistics. External quantum efficiency data are plotted in Figure 7b. Note that, among the SAM and SHSAM IFLs investigated, the SHSAM OPVs fabricated with ITO/**3:1** exhibit the highest performance metrics, comparable to, or slightly greater than, those for the **PEDOT:PSS** IFL, followed by OPVs fabricated with ITO/**5:1** and ITO/**1:1** among the heterogeneous ITO/SAMs. For homogeneous ITO/SAMs, the PV performance decreases in the following order: ITO/$\mathbf{C_3F_4} \rightarrow \mathbf{C_6F_4} \rightarrow \mathbf{C_{10}F_4} \rightarrow \mathbf{C_{18}F_4}$.

DISCUSSION

In this section, the relationships between SAM and SHSAM molecular architecture, packing density (Γ), in-film dipolar interactions, work function, charge transport kinetics, and OPV metrics of the corresponding ITO/SAM and SHSAM devices are discussed.

SAM Supersaturation Effects. Electronic properties as indexed by the change in work function ($\Delta\Phi_s$) vary significantly with the experimental ITO/SAM and SHSAM packing density (Γ). In this study, the Γs of all SAMs and SHSAMs reflect essentially maximum packing density since the grafting conditions established from contact angle versus reaction time with control SAM ITO/$\mathbf{C_3F_4}$ are very similar to maximum coverages determined in the previous SAM IFL study.[1] When the work function (Φ_s) is plotted as a function of Γ, a positive correlation is observed (Figure 8a). In general, the $\Delta\Phi_s$ of the ITO/SAMs and SHSAMs versus solvent-cleaned ITO (Φ_s = 4.54 eV) follow the Helmholtz relationship (eq 1).[58−62] Here, the dipole moment μ of an individual

$$\Delta\Phi_s = \frac{\mu\Gamma\cos\theta}{\varepsilon\varepsilon_0} \quad (1)$$

molecule is obtained by DFT while the SAM packing density Γ and tilt angle θ are obtained, as discussed above, from the CV and XRR data, respectively, in conjunction with calculated molecular lengths and experimental film thicknesses (Table 1). We assume that the SAM absolute dielectric constant, $\varepsilon\varepsilon_0$, is proportional to

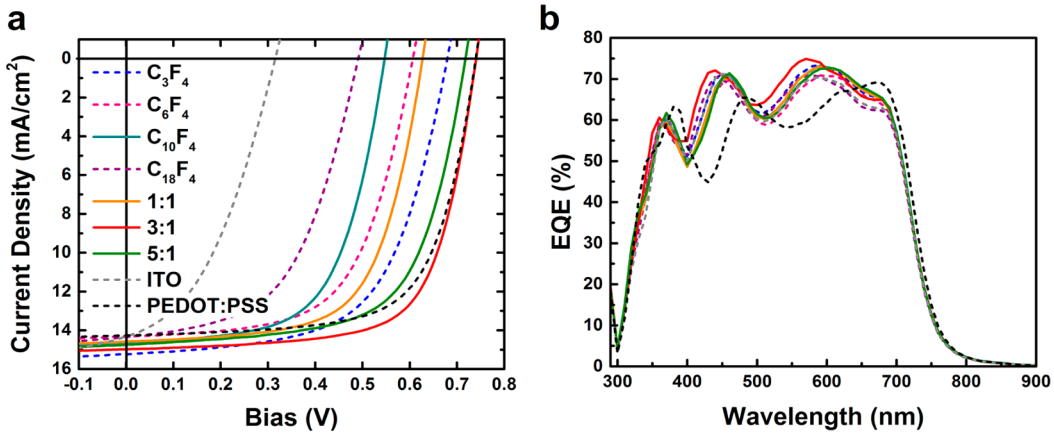

Figure 7. Averaged $J-V$ (a) and EQE (b) plots of ITO/IFL/PTB7:PCBM/LiF/Al OPVs. $\mathbf{C_3F_4}$ (blue dash), $\mathbf{C_6F_4}$ (pink dash), $\mathbf{C_{10}F_4}$ (cyan), $\mathbf{C_{18}F_4}$ (purple dash), **1:1** (orange), **3:1** (red), **5:1** (green), bare ITO (gray dash), and ITO/PEDOT:PSS (black dash) denote the types of anode IFL used.

dx.doi.org/10.1021/ja508453n | J. Am. Chem. Soc. 2014, 136, 17762−17773

Table 3. Device Metrics for PTB7:$PC_{71}BM$-Based Solar Cells Fabricated with the Indicated SAM/SHSAM IFLs[a]

IFL	V_{oc} (mV)	J_{sc} (mA/cm^2)	FF (%)	PCE (%)
C_3F_4	0.680 (±0.016)	15.2 (±0.710)	60.8 (±1.1)	6.25 (±0.39)
C_6F_4	0.591 (±0.041)	14.3 (±0.020)	58.7 (±5.9)	5.30 (±0.14)
$C_{10}F_4$	0.547 (±0.016)	14.6 (±0.085)	61.7 (±0.6)	4.95 (±0.14)
$C_{18}F_4$	0.493 (±0.018)	14.3 (±0.065)	53.5 (±1.1)	3.79 (±0.13)
5:1	0.717 (±0.013)	14.8 (±0.051)	65.0 (±1.2)	6.87 (±0.21)
3:1	0.740 (±0.005)	15.0 (±0.122)	68.7 (±0.5)	7.62 (±0.07), 7.29 (±0.22)[b]
1:1	0.627 (±0.015)	14.6 (±0.041)	64.4 (±0.4)	5.88 (±0.15)
bare ITO	0.316 (±0.022)	14.3 (±0.183)	40.8 (±1.5)	1.85 (±0.19)
PEDOT:PSS	0.744 (±0.003)	14.7 (±0.195)	69.5 (±0.3)	7.55 (±0.13), 7.08 (±0.49)[c]

[a]Tabulated OPV parameters are the average for best 6 devices over 2 substrates. [b]( ) = average of 24 devices over 10 substrates. [c]( ) = average of 24 devices over 6 substrates.

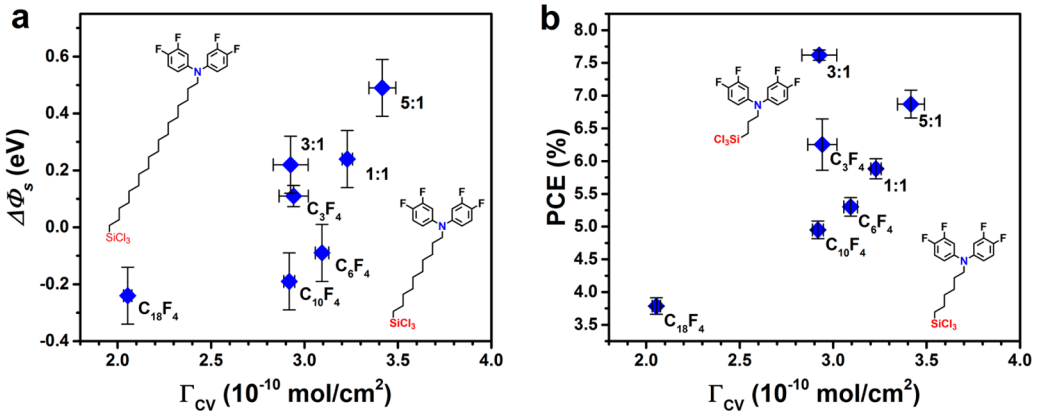

Figure 8. (a) Work functions of ITO/SAM/SHSAMs and (b) power conversion efficiencies (PCEs) of OPVs fabricated from ITO/SAMs/SHSAMs as a function of corresponding cyclic voltammetry determined packing densities. In general, higher IFL packing densities correlate with higher work functions and OPV metrics.

Γ and is similar among all ITO/SAMs.[31] Detailed discussion of SAM dielectric effects is beyond the scope of this study, and is only mentioned briefly.

The primary differences among the homogeneous SAMs are in the chain lengths and Γ values. Since the variation of the homogeneous SAM precursor dipole moments is small (range = 3.62−3.93 D), $\Delta\Phi_s$ might be expected to correlate roughly with Γ. However, as seen in Figure 8a, $\Delta\Phi_s(\Gamma)$ is positive but not strictly linear, and the $\Delta\Phi_s$ of the homogeneous SAMs falls below the line unless corrected for the molecular tilting, $\cos\theta$, eq 1, Supporting Information Figure S13, which is a physically reasonable correction. Note however that this tilting correction cannot be rigorously applied to SHSAMs due to uncertainties in arrangements and compositions.

In contrast to the above results, ITO/SHSAM electronic properties differ distinctly from those of homogeneous ITO/SAMs (Figure 8a). **C_3F_4PAPTSi + $C_{10}F_4$PAPTSi** SHSAMs have greater Γs (Figure 5b) and thus higher Φ_s's, in general accord with eq 1. Interestingly, Figure 8a also reveals that the scaling of $\Delta\Phi_s$ with the approximate SHSAM constituent ratio is nonlinear, reasonably implying that other factors such as intrafilm dipolar interactions also influence $\Delta\Phi_s$, as suggested by Cornil.[63] Since the denser SHSAM architecture permits vertical arraying of headgroups (Figure 3), the effective areal dipole moment (μ_A) can be greater than in homogeneous SAMs, as supported by the computational results in Table 2, where the computed SHSAM μ_As are greater than those of SAMs. The trend in Figure 5b where the ITO/**1:1** and ITO/**5:1** Γs are somewhat greater than that of ITO/**3:1** may be related to dipolar interactions among SHSAM constituents.

In-Film Dipolar Interactions. As evident in Figure 8a, ITO/SHSAMs exhibit greater $\Delta\Phi_s(\Gamma)$ slopes than those of homogeneous ITO/SAMs. In general, deviations from linear $\Delta\Phi_s(\Gamma)$ slopes in eq 1 are thought to reflect factors such as anchor group compositional variation,[63] variations in anchor group binding mode to the surface,[64] surface induced molecular geometry changes,[65] and variations in tail group π-conjugation.[62] In this work, an informative aspect of the observed $\Delta\Phi_s(\Gamma)$ trend is the ITO/**$C_{10}F_4$** and ITO/**3:1** data in which the Γs are experimentally indistinguishable while the $\Delta\Phi_s$ values differ by 0.4 ± 0.2 eV (Table 2). This deviation could, in principle, originate from the in-film dipolar interactions due to the SHSAM structure. In a related heterogeneous SAM study, Niwa[48] and Yasutomi[49] reported denser SAMs along with enhanced redox rates arising from intermolecular dipolar interactions in helical polypeptide SAMs. Lateral dipole−dipole interactions arise from polypeptides having opposite dipolar orientations with respect to their surface anchors, affording denser films and diminished tilt angles. In the present study, enhanced Γ and $\Delta\Phi_s$ are also observed along with the change in SAM composition; however, unlike other studies, the anchor and headgroups here are identical but have tails of different dimensions. Hence, the disposition of the SHSAM dipolar moieties likely favors vertical dipolar coupling which would enhance $\Delta\Phi_s$'s further, while coupling in the Niwa and Yasutomi heterogeneous SAMs is lateral. Additional discussion regarding the in-film dipolar interactions by simulating the SAM and SHSAM structures is available in the Supporting Information (S21)

IFL Effects on OPV Performance. The metrics for the present ITO/SAM or SHSAM IFL/PTB7:$PC_{71}BM$/LiF/Al

dx.doi.org/10.1021/ja508453n | J. Am. Chem. Soc. 2014, 136, 17762−17773

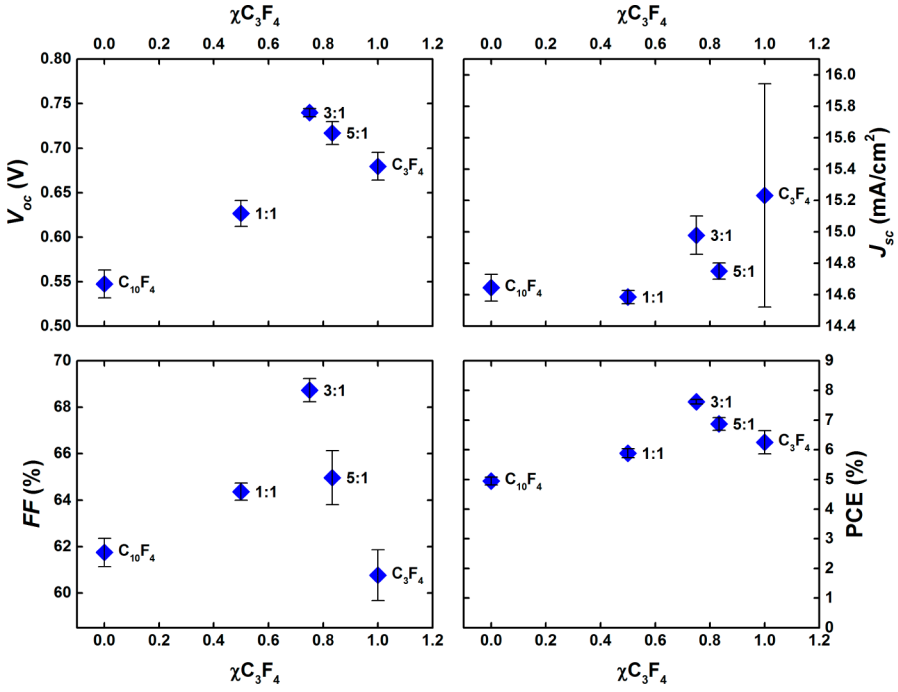

Figure 9. OPV metrics plotted vs solution mole fraction of **C_3F_4PAPTSi** in SHSAM IFLs. SHSAMs based on the ITO/**3:1** and ITO/**5:1** afford higher OPV metrics than either of the homogeneous ITO/**C_3F_4**- or ITO/ **$C_{10}F_4$**-based IFLs.

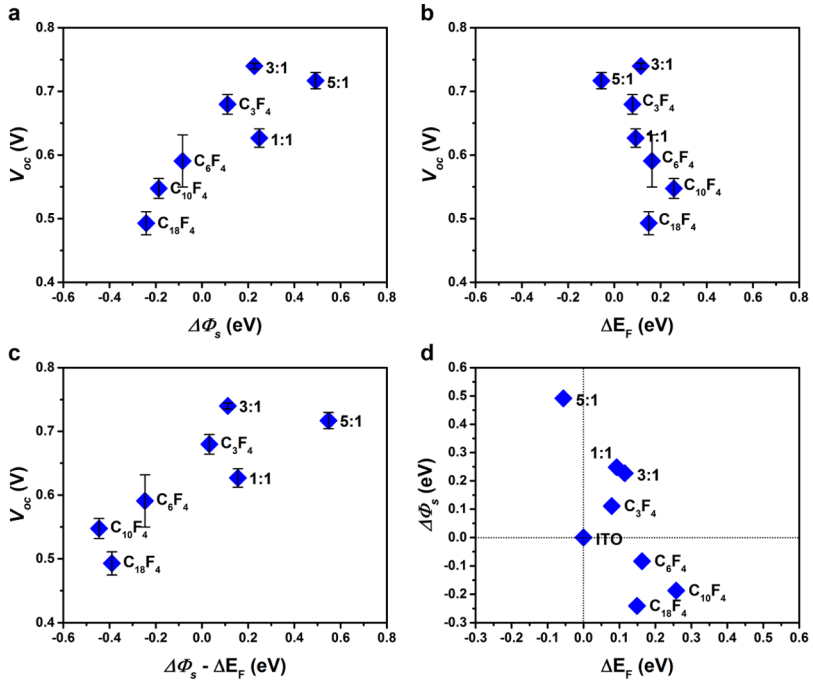

Figure 10. Plots of V_{oc} against work function shift (a), Fermi level shift (b), non-Fermi level component of the work function shift (c), and work function shift against Fermi level shift (d). Note the positive correlation between work function shift and V_{oc}. The dotted line in part d is a guide to distinguish Fermi level shift and work function shift versus those of bare ITO.

OPVs generally track SAM packing (Figure 8b) with positive correlations of V_{oc}, J_{sc}, FF, and PCE as a function of Γ.[1] However, deviations are observed for **3:1**-based OPVs, which exhibit greater performance versus other SAM-based OPVs having comparable Γs. This suggests that factors such as μ_A may influence performance. Dipolar effects are especially noticeable when the ITO/SHSAM-based OPV metrics are plotted versus **C_3F_4PAPTSi:$C_{10}F_4$PAPTSi** ratios along with ITO/SAM-based OPVs; thus, ITO/**3:1**- and ITO/**5:1**-based OPV metrics exceed those of the ITO/**C_3F_4**- and ITO/**$C_{10}F_4$**-based OPVs (Figure 9). If Γ were the dominant determinant of OPV metrics, then the ITO/**3:1**-based OPVs would have lowest metrics among ITO/SHSAM devices. The synergistic effect of mixing **$C_{10}F_4$PAPTSi** + **C_3F_4PAPTSi** evident in Figure 9 suggests additional factors, possibly μ_A. Specifically, the combined effects of the supersaturated Γ and attendant change in μ_A plausibly increase the

dx.doi.org/10.1021/ja508453n | J. Am. Chem. Soc. 2014, 136, 17762−17773

surface potential[66,67] to enhance anode hole collection and charge selection.[1,2,67]

A positive correlation between the $\Delta\Phi_s$ and the ITO/SAM or SHSAM-based OPV V_{oc} values is also observed (Figure 8a), implying interfacial energetic effects originating from surface potential. Since Φ_s is the energy gap between Fermi level (E_F) and the vacuum level, $\Delta\Phi_s$ can originate from changes in the vacuum level, E_F, or both.[68] Vacuum level changes are close to the surface potential,[69,70] which can be altered by densely packed dipolar adsorbates and inferred from $\Delta\Phi_s$ (eq 1, Figure 10),[66,67,71] while E_F changes can be measured by UPS from the pristine substrate VBM.[56,72] Grafting a SAM onto a substrate yields a new surface state VBM (Supporting Information Figure S8), typically with a lower binding energy than for the pristine substrate.[56,73,74] Furthermore, the substrate bulk band structure (VB_{SB}) is largely unaffected by such surface modifications.[56,68] Thus, a shift in VB_{SB} with respect to the pristine substrate indicates a Fermi level displacement (ΔE_F),[42] as observed here for the ITO/SAMs and SHSAMs (Tables 2 and 4), where VB_{SB} values differ from the pristine ITO VBM (3.01 eV). Ionization potential offers another way to monitor ΔE_F. Constant IP signifies $\Delta\Phi_s$ originating from ΔE_F, which is not observed in this study (Figure 6). Therefore, by subtracting ΔE_F from $\Delta\Phi_s$, the surface potential component can be obtained (Table 4).[56,72] When $\Delta\Phi_s$ is plotted against ΔE_F (Figure 10d), the correlation has a steep slope (~2), signifying both ΔE_F and surface potential contribute to $\Delta\Phi_s$. The surface potential subsequently affects energy levels of the active layer blend, commonly assigned to band bending in the space charge region that propagates several nanometers from the surface into the bulk.[67,75,76] Such effects in organic semiconductors have been extensively measured and discussed elsewhere.[27,77−80]

Table 4. Shifts in ITO/SAM/SHSAM Band Structure Energetics and Corresponding OPV V_{oc} Values

surface type	$\Delta\Phi_s$ (eV)	ΔE_F (eV)	$\Delta\Phi_s - \Delta E_F$ (eV)	V_{oc} (V)
ITO	0.00	0.00	0.00	0.316 (±0.022)
C_3F_4	0.08	0.11	0.03	0.680 (±0.016)
C_6F_4	0.16	−0.08	−0.25	0.591 (±0.041)
$C_{10}F_4$	0.26	−0.19	−0.45	0.547 (±0.016)
$C_{18}F_4$	0.15	−0.24	−0.39	0.493 (±0.018)
5:1	0.09	0.25	0.16	0.717 (±0.013)
3:1	0.11	0.23	0.11	0.740 (±0.005)
1:1	−0.06	0.49	0.55	0.627 (±0.015)

At the OPV anode, charge selectivity can be enhanced/reduced as the charge injection barrier height increases/decreases, which is manifested by V_{oc} changes.[27,71,81] Indeed, increased OPV V_{oc}'s are commonly observed with electrode interfacial modification,[1−3,47,82,83] (Table 4) and generally associated with increased charge extraction/suppressed carrier recombination rates; charge extraction rates are closely related to Schottky barrier heights controlled by the surface potential as evident in Figure 10c.[82,84−91] Because of the film dipole direction and resulting surface potential, the PTB7:$PC_{71}BM$ space charge region would be depleted as observed by Lange[80] and Kirchartz.[78] Note that the Schottky barrier height is directly proportional to the difference between energy levels.[27,71,92] As band bending reduces energy difference between ITO E_F and PTB7 HOMO, hole injection into ITO would cost less energy. Conversely, band bending of $PC_{71}BM$ would result in an increased energy level difference, which in turn increases the Schottky barrier height for reverse saturation current yielding less charge leakage.[82,92,93] Therefore, a larger film dipole would be desirable to further enhance OPV metrics. Note that the V_{oc}'s are also observed to be inversely proportional to change in ΔE_F accordance to other studies (Figure 10b),[94−96] however the surface potential effect is greater here. Interestingly, the electrochemically derived heterogeneous electron transport rate constants (k_s's) of the present ITO/SAMs and SHSAMs do not correlate strongly with the corresponding OPV PCEs (Supporting Information Figure S15), possibly due to the measurement method. Further discussion is included in the Supporting Information (S22).

Finally, note the that performance of the ITO/**3:1**-based OPVs rivals or exceeds that of the corresponding **PEDOT:PSS**-based OPVs (Table 3); for conventional architecture BHJ OPVs with ITO anodes, few hole-collecting IFLs are known to outperform PEDOT:PSS.[2,97−100] We expect the supersaturation principle reported in this work is applicable to inverted BHJ OPVs with adequate IFL dipole vectors as well.

CONCLUSIONS

Organosilane SAM precursors of differing tail lengths (Ar_2N-$(CH_2)_n$-$SiCl_3$ with Ar = 3,4-difluorophenyl, n = 3, 6, 10, and 18) are grafted onto oxide surfaces to form stable homogeneous and mixed precursor heterogeneous redox-active (SHSAM) interfacial layers. Characterization by CA, AFM, XRR, XPS, UPS, CV, and DFT analysis shows that the headgroup density in the SHSAMs is increased ("supersaturated") by as much as 17% over homogeneous SAMs. For SHSAMs, differences in tail lengths permit denser headgroup packing and promote vertical in-film dipolar interactions. Consequently, enhanced work functions (by as much as 16%) and areal dipole moments (by as much as 49% from simulated SAMs) are observed. BHJ OPVs fabricated with SHSAM-modified ITO substrates have significantly enhanced OPV metrics versus those fabricated with conventional homogeneous SAMs. The optimal mixed SHSAM precursor molar ratio yielding highest OPV performance is ~3:1 **C_3F_4PAPTSi:$C_{10}F_4$PAPTSi**, and the ITO/**3:1**-OPV performance metrics rival or exceed those of comparable **PEDOT:PSS**-based OPVs. The mechanism underlying the enhanced IFL performance is ascribed to enhanced hole collection and selectivity due to increased surface potential. The ITO/SAM versus ITO/SHSAM work function shift originates primarily from the surface potential imposed by dipolar SAMs. This heterogeneous SAM grafting approach suggests broad potential in technologies as diverse as organic thin-film transistors,[7,81,101] light-emitting diodes,[10,11,102] nanoparticle functionalization,[103−105] and chemical sensing.[14,17,103−108]

ASSOCIATED CONTENT

Supporting Information

Details of SAM precursor synthesis and molecular characterization, SAM grafting procedures and characterization methods, BHJ OPV architecture, computational SAM simulation, XPS, CA, UPS, OPV measurement data and analyses, as well as additional results and discussion. This material is available free of charge via the Internet at http://pubs.acs.org.

AUTHOR INFORMATION

Corresponding Authors

l-chen@northwestern.edu
ratner@northwestern.edu
bedzyk@northwestern.edu

r-chang@northwestern.edu
m-hersam@northwestern.edu
t-marks@northwestern.edu

Notes

The authors declare no competing financial interest.

■ ACKNOWLEDGMENTS

This research was supported in part by the Argonne-Northwestern Solar Energy Research (ANSER) Center, an Energy Frontier Research Center funded by the U.S. Department of Energy, Office of Science under Award Number DE-SC0001059 (N.Z.), and by Office of Basic Energy Sciences under Grant DE-FG02-08ER46536 (C.K.S.). This research was also supported in part by the Northwestern Materials Research Science & Engineering Center (MRSEC) funded by National Science Foundation (NSF) under Grant DMR-1121262 (L.Z.), by an NSF Graduate Research Fellowship (K.A.L.), and by the National Defense Science & Engineering Graduate Fellowship (NDSEG) Program funded by the Department of Defense (DoD) (H.M.H.). The Institute for Sustainability and Energy at Northwestern (ISEN) supplied partial equipment funding. We thank the IMSERC for molecular characterization facilities (NMR) and HRMS work by staff supported by Northwestern University, National Science Foundation (NSF) under NSF CHE-0923236 and CHE-9871268 (1998), Pfizer, and the State of Illinois. We also thank the NIFTI and KECK-II facilities of NUANCE Center for surface characterization (AFM, XPS, and UPS) supported by Northwestern University, the State of Illinois, the Keck foundation, NSF-MRSEC (DMR-1121262), and NSF-NSEC. We thank the J. B. Cohen X-ray Diffraction Facility (XRR) supported by the NSF-MRSEC as well. Finally, we thank J.T. Shin, A. White, M. Butler, J. L. Song, Dr. B. Savoie, Dr. K. Matte, Dr. J. Smith, Dr. S. Yoon, Dr. K.-J. Baeg, Dr. M.-G. Kim, and Prof. T. O. Mason for helpful discussions.

■ REFERENCES

(1) Song, C. K.; White, A. C.; Zeng, L.; Leever, B. J.; Clark, M. D.; Emery, J. D.; Lou, S. J.; Timalsina, A.; Chen, L. X.; Bedzyk, M. J.; Marks, T. J. *ACS Appl. Mater. Interfaces* **2013**, *5*, 9224−9240.
(2) Ratcliff, E. L.; Garcia, A.; Paniagua, S. A.; Cowan, S. R.; Giordano, A. J.; Ginley, D. S.; Marder, S. R.; Berry, J. J.; Olson, D. C. *Adv. Energy Mater.* **2013**, *3*, 647−656.
(3) Beaumont, N.; Hancox, I.; Sullivan, P.; Hatton, R. A.; Jones, T. S. *Energy Environ. Sci.* **2011**, *4*, 1708−1711.
(4) Hau, S. K.; Yip, H.-L.; Ma, H.; Jen, A. K.-Y. *Appl. Phys. Lett.* **2008**, *93*, 233304/1−233304/3.
(5) Hains, A. W.; Liu, J.; Martinson, A. B. F.; Irwin, M. D.; Marks, T. J. *Adv. Funct. Mater.* **2010**, *20*, 595−606.
(6) Hains, A. W.; Ramanan, C.; Irwin, M. D.; Liu, J.; Wasielewski, M. R.; Marks, T. J. *ACS Appl. Mater. Interfaces* **2010**, *2*, 175−185.
(7) DiBenedetto, S. A.; Facchetti, A.; Ratner, M. A.; Marks, T. J. *Adv. Mater.* **2009**, *21*, 1407−1433.
(8) Schmaltz, T.; Amin, A. Y.; Khassanov, A.; Meyer-Friedrichsen, T.; Steinruck, H. G.; Magerl, A.; Segura, J. J.; Voitchovsky, K.; Stellacci, F.; Halik, M. *Adv. Mater.* **2013**, *25*, 4511−4514.
(9) Youn, J.; Dholakia, G. R.; Huang, H.; Hennek, J. W.; Facchetti, A.; Marks, T. J. *Adv. Funct. Mater.* **2012**, *22*, 1856−1869.
(10) Huang, Q.; Li, J.; Evmenenko, G. A.; Dutta, P.; Marks, T. J. *Chem. Mater.* **2006**, *18*, 2431−2442.
(11) Hotchkiss, P. J.; Jones, S. C.; Paniagua, S. A.; Sharma, A.; Kippelen, B.; Armstrong, N. R.; Marder, S. R. *Acc. Chem. Res.* **2012**, *45*, 337−346.
(12) Huang, Q. L.; Li, J. F.; Marks, T. J.; Evmenenko, G. A.; Dutta, P. *J. Appl. Phys.* **2007**, *101*, 093101/1−093101/13.
(13) Huang, Q.; Evmenenko, G. A.; Dutta, P.; Lee, P.; Armstrong, N. R.; Marks, T. J. *J. Am. Chem. Soc.* **2005**, *127*, 10227−10242.
(14) Mandler, D.; Kraus-Ophir, S. *J. Solid State Electrochem.* **2011**, *15*, 1535−1558.
(15) Xu, P. C.; Li, X. X.; Yu, H. T.; Liu, M.; Li, J. G. *J. Micromech. Microeng.* **2010**, *20*, 1−6.
(16) Mandal, H. S.; Kraatz, H. B. *Chem. Phys.* **2006**, *326*, 246−251.
(17) Choi, I.; Yeo, W. S. *ChemPhysChem* **2013**, *14*, 55−69.
(18) Chaki, N. K.; Vijayamohanan, K. *Biosens. Bioelectron.* **2002**, *17*, 1−12.
(19) Bong, J.; Kim, D. H.; Kim, H.; Lee, S. S.; Ju, S. *Appl. Phys. Express* **2013**, *6*, 127003/1−127003/4.
(20) Srinivasan, U.; Houston, M. R.; Howe, R. T.; Maboudian, R. *J. Microelectromech. Syst.* **1998**, *7*, 252−260.
(21) Cheng, J.; Robinson, D. B.; Cicero, R. L.; Eberspacher, T.; Barrelet, C. J.; Chidsey, C. E. D. *J. Phys. Chem. B* **2001**, *105*, 10900−10904.
(22) Li, Y.; Moon, K. S.; Wong, C. P. *J. Electron. Mater.* **2005**, *34*, 266−271.
(23) Ishida, T.; Mizutani, W.; Aya, Y.; Ogiso, H.; Sasaki, S.; Tokumoto, H. *J. Phys. Chem. B* **2002**, *106*, 5886−5892.
(24) Paniagua, S. A.; Hotchkiss, P. J.; Jones, S. C.; Marder, S. R.; Mudalige, A.; Marrikar, F. S.; Pemberton, J. E.; Armstrong, N. R. *J. Phys. Chem. C* **2008**, *112*, 7809−7817.
(25) Wobkenberg, P. H.; Ball, J.; Kooistra, F. B.; Hummelen, J. C.; de Leeuw, D. M.; Bradley, D. D. C.; Anthopoulos, T. D. *Appl. Phys. Lett.* **2008**, *93*, 013303/1−013303/3.
(26) You, Z. Z. *Mater. Lett.* **2007**, *61*, 3809−3814.
(27) MacLeod, B. A.; Horwitz, N. E.; Ratcliff, E. L.; Jenkins, J. L.; Armstrong, N. R.; Giordano, A. J.; Hotchkiss, P. J.; Marder, S. R.; Campbell, C. T.; Ginger, D. S. *J. Phys. Chem. Lett.* **2012**, *3*, 1202−1207.
(28) Veinot, J. G. C.; Marks, T. J. *Acc. Chem. Res.* **2005**, *38*, 632−643.
(29) Eckermann, A. L.; Feld, D. J.; Shaw, J. A.; Meade, T. J. *Coord. Chem. Rev.* **2010**, *254*, 1769−1802.
(30) Chidsey, C. E. D.; Bertozzi, C. R.; Putvinski, T. M.; Mujsce, A. M. *J. Am. Chem. Soc.* **1990**, *112*, 4301−4306.
(31) Romaner, L.; Heimel, G.; Ambrosch-Draxl, C.; Zojer, E. *Adv. Funct. Mater.* **2008**, *18*, 3999−4006.
(32) Yip, H.-L.; Hau, S. K.; Baek, N. S.; Ma, H.; Jen, A. K.-Y. *Adv. Mater.* **2008**, *20*, 2376−2382.
(33) Steim, R.; Kogler, F. R.; Brabec, C. J. *J. Mater. Chem.* **2010**, *20*, 2499−2512.
(34) Hau, S. K.; Cheng, Y.-J.; Yip, H.-L.; Zhang, Y.; Ma, H.; Jen, A. K.-Y. *ACS Appl. Mater. Interfaces* **2010**, *2*, 1892−1902.
(35) Berggren, C.; Stalhandske, P.; Brundell, J.; Johansson, G. *Electroanalysis* **1999**, *11*, 156−160.
(36) Sabatani, E.; Cohen-Boulakia, J.; Bruening, M.; Rubinstein, I. *Langmuir* **1993**, *9*, 2974−2981.
(37) Chailapakul, O.; Crooks, R. M. *Langmuir* **1995**, *11*, 1329−1340.
(38) Li, Y. *Open Photovoltaics Analysis Platform (OPVAP)*. 2011; Available from: opvap.com/eqe.php.
(39) Perales, J. B.; Van Vranken, D. L. *J. Org. Chem.* **2001**, *66*, 7270−7274.
(40) Wang, Y. L.; Lieberman, M. *Langmuir* **2003**, *19*, 1159−1167.
(41) Owens, D. K.; Wendt, R. C. *J. Appl. Polym. Sci.* **1969**, *13*, 1741.
(42) Vacca, P.; Petrosino, M.; Miscioscia, R.; Nenna, G.; Minarini, C.; Della Sala, D.; Rubino, A. *Thin Solid Films* **2008**, *516*, 4232−4237.
(43) Armstrong, N. R.; Carter, C.; Donley, C.; Simmonds, A.; Lee, P.; Brumbach, M.; Kippelen, B.; Domercq, B.; Yoo, S. *Thin Solid Films* **2003**, *445*, 342−352.
(44) Badre, C.; Pauporte, T.; Turmine, M.; Lincot, D. *Superlattices Microstruct.* **2007**, *42*, 99−102.
(45) Kim, J. S.; Park, J. H.; Lee, J. H.; Jo, J.; Kim, D.-Y.; Cho, K. *Appl. Phys. Lett.* **2007**, *91*, 112111/1−112111/3.
(46) Cui, J.; Huang, Q.; Veinot, J. G. C.; Yan, H.; Marks, T. J. *Adv. Mater.* **2002**, *14*, 565−569.
(47) Khodabakhsh, S.; Sanderson, B. M.; Nelson, J.; Jones, T. S. *Adv. Funct. Mater.* **2006**, *16*, 95−100.

(48) Niwa, M.; Morikawa, M.; Higashi, N. *Angew. Chem., Int. Ed.* **2000**, *39*, 960−963.
(49) Yasutomi, S.; Morita, T.; Imanishi, Y.; Kimura, S. *Science* **2004**, *304*, 1944−1947.
(50) Miyake, K.; Hori, Y.; Ikeda, T.; Asakawa, M.; Shimizu, T.; Sasaki, S. *Langmuir* **2008**, *24*, 4708−4714.
(51) Natan, A.; Kuritz, N.; Kronik, L. *Adv. Funct. Mater.* **2010**, *20*, 2077−2084.
(52) Pavlishchuk, V. V.; Addison, A. W. *Inorg. Chim. Acta* **2000**, *298*, 97−102.
(53) Cardona, C. M.; Li, W.; Kaifer, A. E.; Stockdale, D.; Bazan, G. C. *Adv. Mater.* **2011**, *23*, 2367−2371.
(54) Yi, Y.; Lyon, J. E.; Beerbom, M. M.; Schlaf, R. *J. Appl. Phys.* **2006**, *100*, 093719/1−093719/7.
(55) Cho, S.; Seo, J. H.; Lee, K.; Heeger, A. J. *Adv. Funct. Mater.* **2009**, *19*, 1459−1464.
(56) Schroeder, P. G.; France, C. B.; Park, J. B.; Parkinson, B. A. *J. Phys. Chem. B* **2003**, *107*, 2253−2261.
(57) Liang, Y.; Xu, Z.; Xia, J.; Tsai, S.-T.; Wu, Y.; Li, G.; Ray, C.; Yu, L. *Adv. Mater.* **2010**, *22*, 1−4.
(58) Oliveira, O. N.; Taylor, D. M.; Lewis, T. J.; Salvagno, S.; Stirling, C. J. M. *J. Chem. Soc., Faraday Trans.* **1989**, *85*, 1009−1018.
(59) Bruening, M.; Cohen, R.; Guillemoles, J. F.; Moav, T.; Libman, J.; Shanzer, A.; Cahen, D. *J. Am. Chem. Soc.* **1997**, *119*, 5720−5728.
(60) Paska, Y.; Haick, H. *J. Phys. Chem. C* **2009**, *113*, 1993−1997.
(61) Kornblum, L.; Paska, Y.; Haick, H.; Eizenberg, M. *J. Phys. Chem. C* **2013**, *117*, 233−237.
(62) Aqua, T.; Cohen, H.; Sinai, O.; Frydman, V.; Bendikoy, T.; Krepel, D.; Hod, O.; Kronik, L.; Naaman, R. *J. Phys. Chem. C* **2011**, *115*, 24888−24892.
(63) Cornil, D.; Cornil, J. *J. Electron Spectrosc. Relat. Phenom.* **2013**, *189*, 32−38.
(64) Wood, C.; Li, H.; Winget, P.; Bredas, J. L. *J. Phys. Chem. C* **2012**, *116*, 19125−19133.
(65) Koch, N.; Gerlach, A.; Duhm, S.; Glowatzki, H.; Heimel, G.; Vollmer, A.; Sakamoto, Y.; Suzuki, T.; Zegenhagen, J.; Rabe, J. P.; Schreiber, F. *J. Am. Chem. Soc.* **2008**, *130*, 7300−7304.
(66) Monti, O. L. A. *J. Phys. Chem. Lett.* **2012**, *3*, 2342−2351.
(67) Vaynzof, Y.; Kabra, D.; Zhao, L. H.; Ho, P. K. H.; Wee, A. T. S.; Friend, R. H. *Appl. Phys. Lett.* **2010**, *97*, 033309.
(68) Klein, A.; Korber, C.; Wachau, A.; Sauberlich, F.; Gassenbauer, Y.; Harvey, S. P.; Proffit, D. E.; Mason, T. O. *Materials* **2010**, *3*, 4892−4914.
(69) Smith, J. R. *Phys. Rev.* **1969**, *181*, 522−529.
(70) Lang, N. D.; Kohn, W. *Phys. Rev. B* **1971**, *3*, 1215−1223.
(71) Ishii, H.; Sugiyama, K.; Ito, E.; Seki, K. *Adv. Mater.* **1999**, *11*, 605.
(72) Manandhar, K.; Parkinson, B. A. *J. Phys. Chem. C* **2012**, *116*, 19379−19384.
(73) Greiner, M. T.; Helander, M. G.; Tang, W. M.; Wang, Z. B.; Qiu, J.; Lu, Z. H. *Nat. Mater.* **2012**, *11*, 76−81.
(74) Alloway, D. M.; Hofmann, M.; Smith, D. L.; Gruhn, N. E.; Graham, A. L.; Colorado, R.; Wysocki, V. H.; Lee, T. R.; Lee, P. A.; Armstrong, N. R. *J. Phys. Chem. B* **2003**, *107*, 11690−11699.
(75) Lange, I.; Blakesley, J. C.; Frisch, J.; Vollmer, A.; Koch, N.; Neher, D. *Phys. Rev. Lett.* **2011**, *106*, 216402/1−216402/4.
(76) Zhang, Z.; Yates, J. T. *Chem. Rev.* **2012**, *112*, 5520−5551.
(77) Kemerink, M.; Kramer, J. M.; Gommans, H. H. P.; Janssen, R. A. J. *Appl. Phys. Lett.* **2006**, *88*, 192108.
(78) Kirchartz, T.; Gong, W.; Hawks, S. A.; Agostinelli, T.; MacKenzie, R. C. I.; Yang, Y.; Nelson, J. *J. Phys. Chem. C* **2012**, *116*, 7672−7680.
(79) Guerrero, A.; Montcada, N. F.; Ajuria, J.; Etxebarria, I.; Pacios, R.; Garcia-Belmonte, G.; Palomares, E. *J. Mater. Chem. A* **2013**, *1*, 12345−12354.
(80) Lange, I.; Kniepert, J.; Pingel, P.; Dumsch, I.; Allard, S.; Janietz, S.; Scherf, U.; Neher, D. *J. Phys. Chem. Lett.* **2013**, *4*, 3865−3871.
(81) Natali, D.; Caironi, M. *Adv. Mater.* **2012**, *24*, 1357−1387.
(82) Knesting, K. M.; Ju, H. X.; Schlenker, C. W.; Giordano, A. J.; Garcia, A.; Smith, O. L.; Olson, D. C.; Marder, S. R.; Ginger, D. S. *J. Phys. Chem. Lett.* **2013**, *4*, 4038−4044.
(83) Luck, K. A.; Shastry, T. A.; Loser, S.; Ogien, G.; Marks, T. J.; Hersam, M. C. *Phys. Chem. Chem. Phys.* **2013**, *15*, 20966−20972.
(84) Kirchartz, T.; Pieters, B. E.; Taretto, K.; Rau, U. *J. Appl. Phys.* **2008**, *104*, 094513/1−094513/9.
(85) Wagenpfahl, A.; Deibel, C.; Dyakonov, V. *IEEE J. Sel. Top. Quantum Electron.* **2010**, *16*, 1759−1763.
(86) Bisquert, J.; Zaban, A.; Greenshtein, M.; Mora-Sero, I. *J. Am. Chem. Soc.* **2004**, *126*, 13550−13559.
(87) Bisquert, J.; Garcia-Belmonte, G. *J. Phys. Chem. Lett.* **2011**, *2*, 1950−1964.
(88) Dasgupta, B.; Goh, W. P.; Ooi, Z. E.; Wong, L. M.; Jiang, C. Y.; Ren, Y.; Tok, E. S.; Pan, J.; Zhang, J.; Chiam, S. Y. *J. Phys. Chem. C* **2013**, *117*, 9206−9211.
(89) Qi, B. Y.; Wang, J. Z. *Phys. Chem. Chem. Phys.* **2013**, *15*, 8972−8982.
(90) Tress, W.; Leo, K.; Riede, M. *Phys. Rev. B* **2012**, *85*, 155201/1−155201/11.
(91) Kumar, A.; Lakhwani, G.; Elmalem, E.; Huck, W. T. S.; Rao, A.; Greenham, N. C.; Friend, R. H. *Energy Environ. Sci.* **2014**, 2227−2231.
(92) Sze, S. M. *Physics of Semiconductor Devices*, 2nd ed.; Wiley: New York, 1981.
(93) Lee, W.; Seo, J. H.; Woo, H. Y. *Polymer* **2013**, *54*, 5104−5121.
(94) Potscavage, W. J.; Sharma, A.; Kippelen, B. *Acc. Chem. Res.* **2009**, *42*, 1758−1767.
(95) Deibel, C.; Dyakonov, V. *Rep. Prog. Phys.* **2010**, *73*, 096401/1−096401/39.
(96) Giebink, N. C.; Wiederrecht, G. P.; Wasielewski, M. R.; Forrest, S. R. *Phys. Rev. B* **2010**, *82*, 155305/1−155305/12.
(97) Yuan, Y.; Reece, T. J.; Sharma, P.; Poddar, S.; Ducharme, S.; Gruverman, A.; Yang, Y.; Huang, J. *Nat. Mater.* **2011**, *10*, 296−302.
(98) He, Z. C.; Zhong, C. M.; Su, S. J.; Xu, M.; Wu, H. B.; Cao, Y. *Nat. Photonics* **2012**, *6*, 591−595.
(99) Zhou, Y. H.; Fuentes-Hernandez, C.; Shim, J.; Meyer, J.; Giordano, A. J.; Li, H.; Winget, P.; Papadopoulos, T.; Cheun, H.; Kim, J.; Fenoll, M.; Dindar, A.; Haske, W.; Najafabadi, E.; Khan, T. M.; Sojoudi, H.; Barlow, S.; Graham, S.; Bredas, J. L.; Marder, S. R.; Kahn, A.; Kippelen, B. *Science* **2012**, *336*, 327−332.
(100) Yaacobi-Gross, N.; Treat, N. D.; Pattanasattayavong, P.; Faber, H.; Perumal, A. K.; Stingelin, N.; Bradley, D. D. C.; Stavrinou, P. N.; Heeney, M.; Anthopoulos, T. D. *Adv. Energy Mater.* **2014**, DOI: 10.1002/aenm.201401529.
(101) Chung, Y.; Verploegen, E.; Vailionis, A.; Sun, Y.; Nishi, Y.; Murmann, B.; Bao, Z. *Nano Lett.* **2011**, *11*, 1161−1165.
(102) Wang, M. Q.; Hill, I. G. *Org. Electron.* **2012**, *13*, 498−505.
(103) Harkness, K. M.; Turner, B. N.; Agrawal, A. C.; Zhang, Y. B.; McLean, J. A.; Cliffel, D. E. *Nanoscale* **2012**, *4*, 3843−3851.
(104) Shen, Z. H.; Huang, M. C.; Xiao, C. D.; Zhang, Y.; Zeng, X. Q.; Wang, P. G. *Anal. Chem.* **2007**, *79*, 2312−2319.
(105) Jackson, A. M.; Myerson, J. W.; Stellacci, F. *Nat. Mater.* **2004**, *3*, 330−336.
(106) Berger, R.; Delamarche, E.; Lang, H. P.; Gerber, C.; Gimzewski, J. K.; Meyer, E.; Guntherodt, H. J. *Science* **1997**, *276*, 2021−2024.
(107) White, R. J.; Phares, N.; Lubin, A. A.; Xiao, Y.; Plaxco, K. W. *Langmuir* **2008**, *24*, 10513−10518.
(108) Satjapipat, M.; Sanedrin, R.; Zhou, F. M. *Langmuir* **2001**, *17*, 7637−7644.